Chapter Four

Magnetic Properties: Experimental Results

4.1 Overview

Chapter 3 describes the growth of a series of strained, 7 nm-thick b-axis-oriented Dy films. Two additional films of compressed Dy on Lu, 50 nm and 100 nm thick, were also prepared. The magnetic properties of these samples were determined using SQUID magnetometry. The results of these measurements are presented in this Chapter, which is organized as follows. The first Section describes how magnetization measurements were taken as a function of temperature T. The second Section presents isothermal magnetization measurements taken as a function of H (hysteresis loops). Subsequent Sections present data extracted from these loops, including the strain dependence of magnetic ordering temperatures, critical fields, and coercive fields. Next, measurements of hysteresis loops from previously unmagnetized samples are reported. Finally, time-dependent results of magnetic relaxation measurements are presented.

Owing to the slightly different c/a ratios of Lu and Y, the in-plane strain for b-axis-oriented samples is not isotropic as it is for c-axis-oriented samples. A full characterization of the in-plane strain therefore requires specification of the in-plane a and c strains, e_{11} and e_{33}, as discussed within Chapter Two. For all quantitative calculations involving strain these two strains were considered independently, even though the difference between them is small compared with the largest strains attainable, specifically, e_{11} = -2.2% for Lu

and e_{11} = +1.5% for Y. Unless otherwise indicated, the strain e_{11} is used simply as a label each sample.

4.2 Temperature Dependence of Magnetization

Magnetization *M* was measured as a function of temperature *T*, using the SQUID magnetometers discussed in Chapter 2. When examining a new magnetic material, the magnetization *M(T)* is often the most useful first step to an interpretation of magnetic properties. These measurements identify important processes such as ferromagnetic transitions, and provide estimates of the critical temperatures associated with the magnetic ordering. Further information about magnetic phases such as antiferromagnetism or the paramagnetic Curie temperatures can often be deduced.

The most efficient way to take measurements of temperature-dependent susceptibility is as follows. First, the sample is cooled in zero field to the lowest temperature of interest. In ferromagnets a magnetic domain structure then naturally develops to minimize the internal magnetic energy. A small aligning field is established along the easy axis of magnetization (if known), and the net magnetic moment of the sample is determined as a function of *T*. This is known as the zero-field-cooled (ZFC) leg of the curve *M(T)*. With increasing temperature the moments and domain walls loosen, and this is reflected in the change of net magnetization of the sample. For example, if the sample is ferromagnetic, *M(T)* increases with temperature as the alignment of the moments increases. If the sample is antiferromagnetic but the aligning field has been placed along a direction perpendicular to the magnetization, *M(T)* may be constant. Sharp steps can occur as *M* varies with *T* (not observed in the present work) and these can signal spin-slip behavior in which a ferrimagnetic state is "locked" to a specific **q**-vector until thermal activation causes it to unlock.

Upon reaching the highest desired temperature, the aligning field is maintained and magnetization is measured as the sample is cooled back to the lowest temperature of interest. This is the field-cooled (FC) leg of the curve *M(T)*. If, as in the measurements described here, the sample is heated above the Néel temperature into the paramagnetic

phase, then upon subsequent cooling the magnetization possesses a different, field-aligned domain structure. Superimposed on both the ZFC and FC legs is the equilibrium change in magnetization, which in a mean field theory is described by the Brillouin function. The superposition of these several effects can make the data difficult to analyze.

In the present experiments, samples were oriented, cut to size, and loaded into the SQUID magnetometer as discussed in Chapter 2. The results of ZFC and FC measurements taken for the complete range of b-axis-oriented samples are shown in Figure 4.1. The aligning field was 500 Oe directed along the in-plane $[11\bar{2}0]$ axis; for bulk Dy, the six equivalent $[11\bar{2}0]$ directions are the easy magnetization axes. The data are presented in Figure 4.1 by order of increasing in-plane strain.

The important features of these measurements are indicated in the schematic diagram shown as Figure 4.2. First, all samples exhibit a pronounced rounded cusp in *M(T)* at about 165 K and there is a slow decay of magnetization thereafter. This clearly identifies the Néel temperature T_N at the paramagnetic phase boundary, which is seen to lie below the Néel temperature of bulk Dy (T_N = 178 K).

Second, for most samples there is a well-defined temperature at which a pronounced splitting of the ZFC and FC curves occurs [1]. This marks the onset of irreversibility in the magnetization process. Field-dependent measurements of magnetic hysteresis (presented below) confirm that the samples are ferromagnetic below this temperature. It was observed in this research that the lowest splitting temperature occurs for the sample with near-zero in-plane strain, and the splitting temperature increases as either compressive or tensile strain is applied. This is in marked contrast to the monotonic behavior observed for c-axis-oriented Dy, in which ferromagnetism was suppressed for tensile strain (e.g., Dy on Y) and enhanced for compressive strain (e.g., Dy on Lu).

An important difference among the curves shown in Figure 4.1 is the magnitude of net magnetization attained by each sample. As the strain changes from compressive to tensile, a pronounced peak develops in the ZFC branch and grows in magnitude as the tensile strain is increased. Similarly, the magnetization in the FC leg at the lowest temperature increases in magnitude. It is shown later that these effects derive from a strain-induced transition between different easy axes of magnetization. This forms the

main topic of Chapter 5. Note that the ZFC moment exceeds that in the FC data for some films. This uncommon behavior may originate in the domain structure of these samples [2].

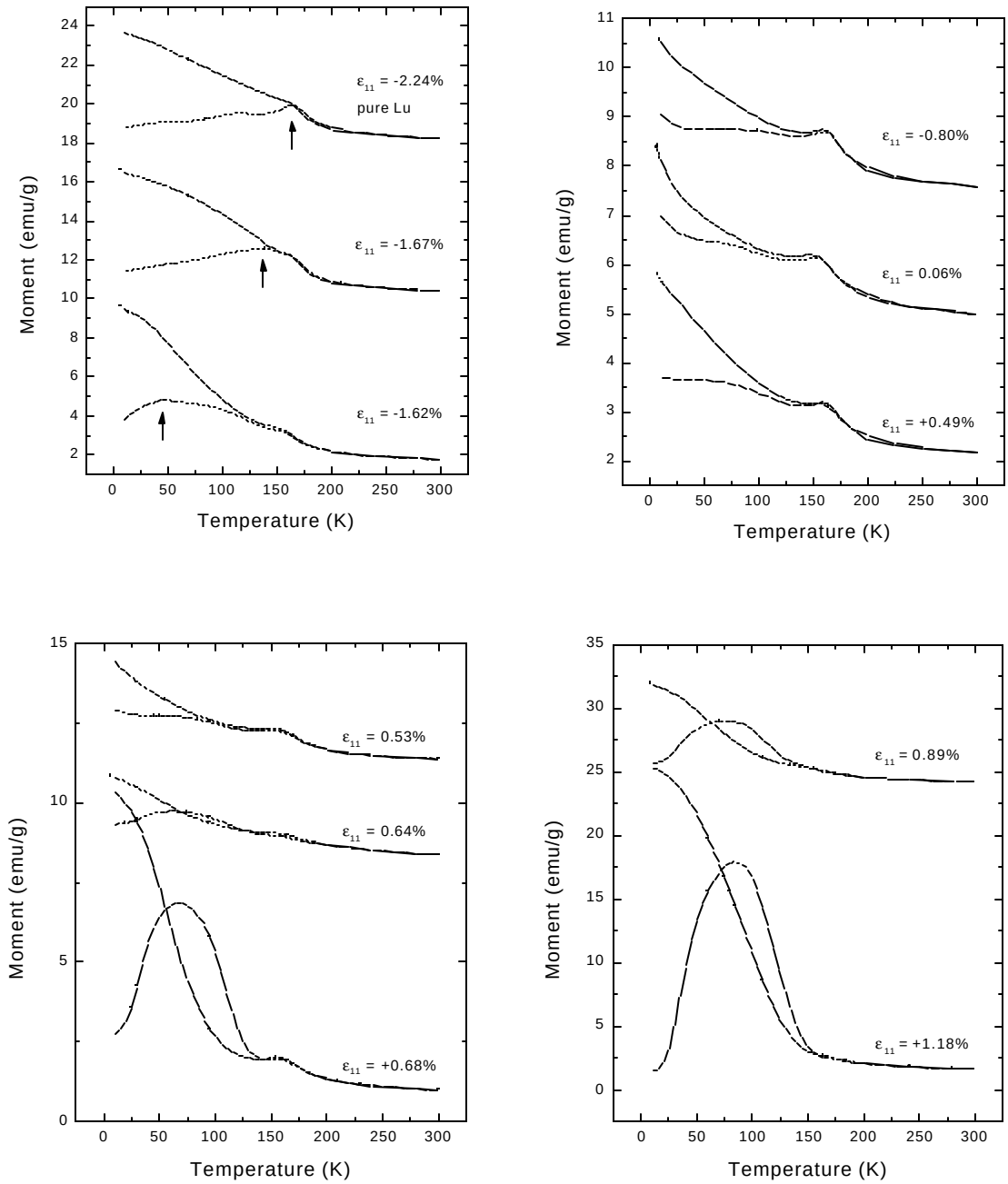

Figure 4.1. The results of ZFC/FC measurements for b-axis-oriented samples. These data are arranged by increasing tensile strain. Note the drastic change in vertical scale required as the limit of tensile strain (growth on pure Y) is approached.

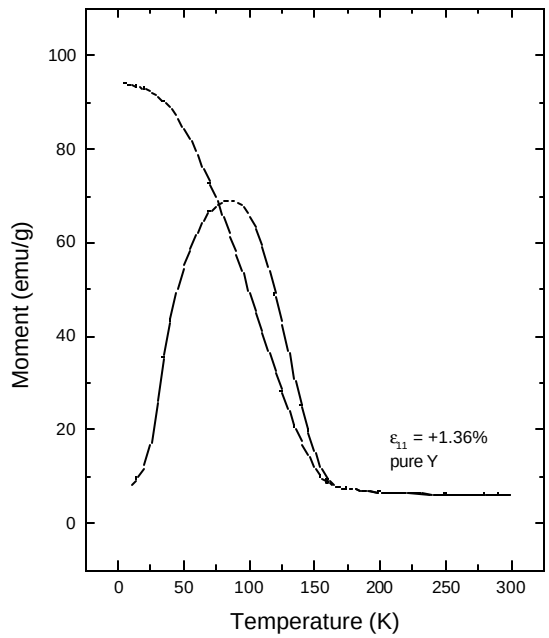

Figure 4.1 - cont'd. For the maximum attainable tensile strain (Dy on pure Y), the moment is large when the field is along the in-plane easy magnetization axis.

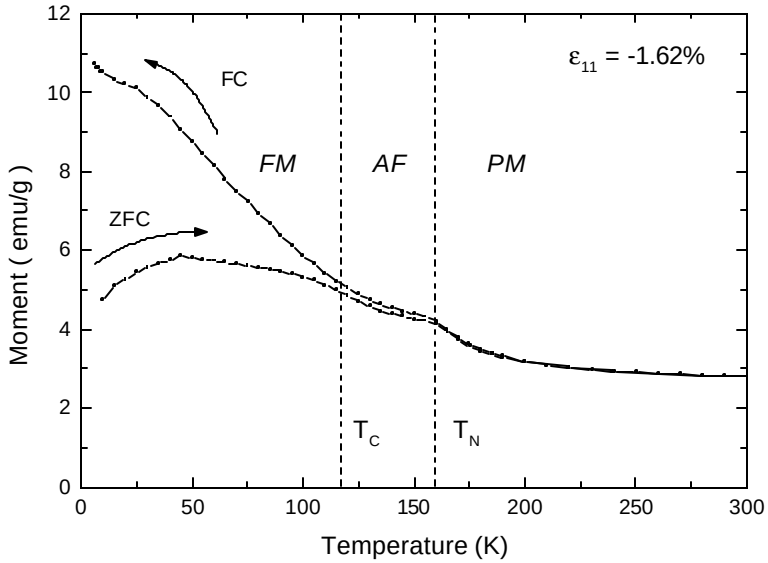

Figure 4.2. The results of a typical ZFC/FC measurement. The critical temperatures and ferromagnetic (FM), antiferromagnetic (AF) and paramagnetic (PM) phases are labeled. The splitting of the ZFC and FC legs observed below T_C is due to the parasitic ferromagnetic contaminant.

The ZFC/FC data described above are not by themselves sufficient to define a complete model for the magnetic behavior of b-axis-oriented Dy. The ZFC/FC splitting clearly demonstrates irreversibility and suggests a ferromagnetic transition; this is corroborated for Dy under tensile strain by the accompanying increase of net magnetization. These inferences are confirmed by observation of a remanent moment in the results presented in the next Section.

4.3 Field Dependence of Magnetization

This Section presents isothermal magnetization data *M(T,H)* collected at a wide range of temperatures. It is primarily from these measurements that a model was developed to describe the magnetic ordering. This model is discussed in Chapter 5.

The measurements were carried out using the 7T SQUID magnetometer as discussed in Chapter 2. Samples were introduced into the instrument and cooled under zero field to the desired temperature. Next, a magnetic field of -7 T was applied and the net magnetization of the sample recorded as the magnetic field was cycled to +7 T in stages and then reduced again to -7 T. Complete hysteresis loops were obtained in this

way. Initial studies indicated that M showed interesting variations with H, for example, near H=0 and near a critical field H_C at which the slope of $M(H)$ changes abruptly. The initial results directed further attention to regions of interest and hysteresis loops were obtained for all samples, each requiring about 5 hours of SQUID time.

As described in Chapter 2, raw SQUID data contain diamagnetic contributions from the sapphire substrate and the sample holder, as well as a small (1%) ferromagnetic background due to an impurity in the Zr buffer layer. The hysteresis loops and other data reported in this chapter have been corrected for both of these effects. Most data for $M(H)$ presented in this chapter were collected with the applied field directed along the in-plane $[11\bar{2}0]$ axis. Measurements that probe the anisotropy, performed with the field along other axes, are presented in Section 4.6. Hysteresis loops which show behavior typical for all samples are presented in Figure 4.3. The important features of these data are indicated in Figure 4.4.

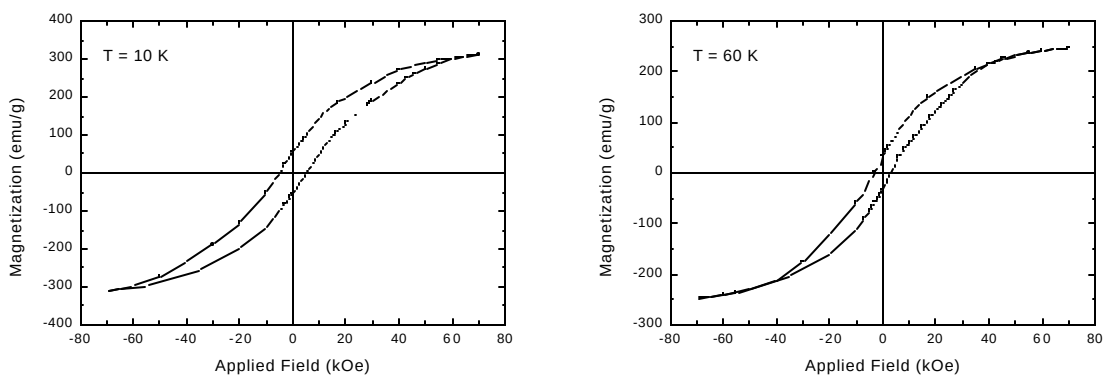

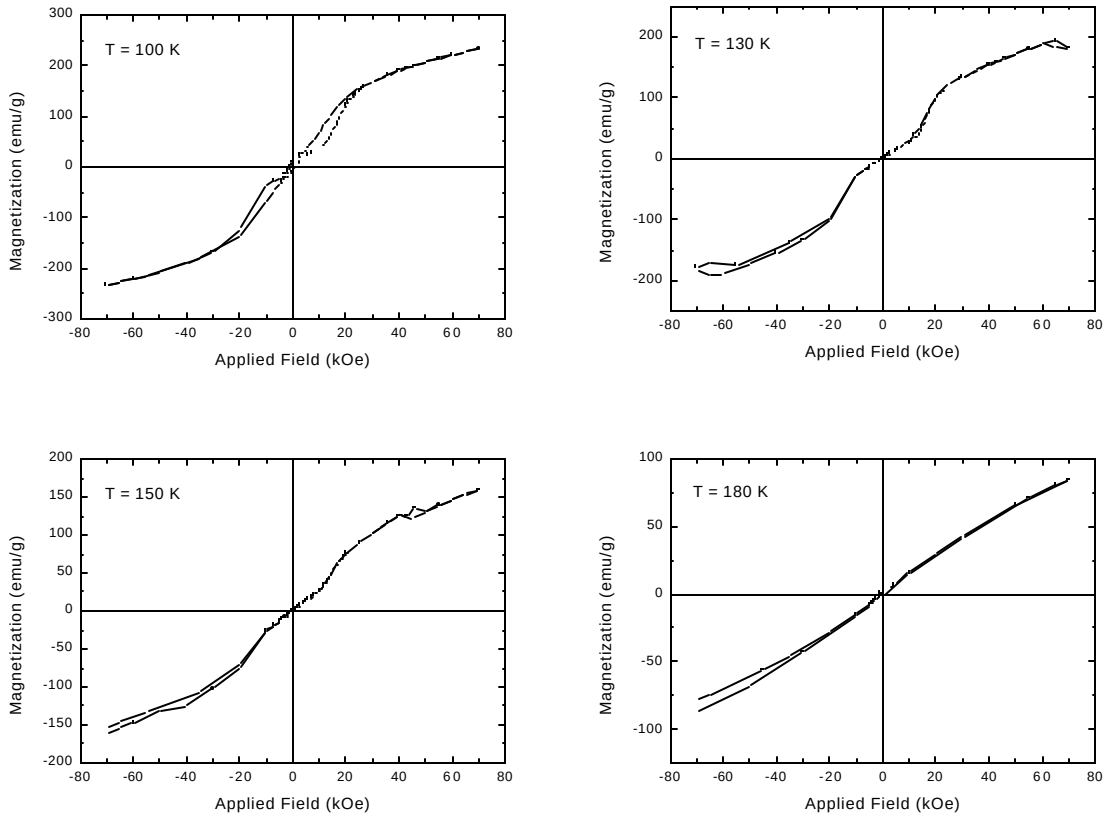

Figure 4.3. Hysteresis loops taken at different temperatures for b-axis-oriented samples grown on pure Lu (ε_{11}=-2.2%). The hysteresis loop becomes wasp-waisted as the remanent magnetization decreases with increasing temperature. Above T_N, the hysteresis disappears and the samples are paramagnetic. The splitting at -7T at high temperature is an experimental artifact (see text).

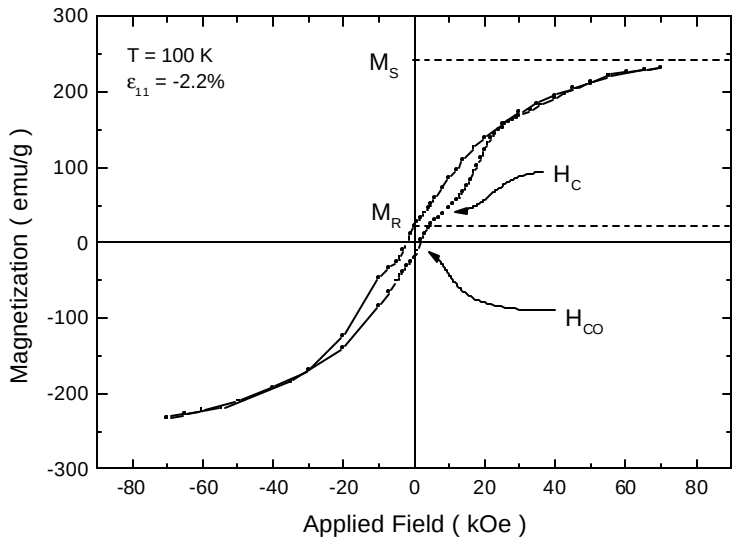

Figure 4.4. The results of typical measurements of *M(H)*. The important fields and magnetization are labeled.

At the lowest temperatures, there is a non-zero, remanent magnetization at zero applied field, confirming that all samples become ferromagnetic. As the temperature is increased, the remanent magnetization and coercive fields are reduced, and the loops acquire a wasp-waisted shape. This shape is exhibited in many systems, and it is commonly associated with a domain collapse mechanism, possibly a fast collapse of one domain followed by a slow depopulation of other domains. Above a critical temperature (T_C) the remanent magnetization disappears and the hysteresis loops are linear and single-valued through the origin. Hysteresis can still be seen at fields greater than a critical field (H_C), indicated by an abrupt inflection in the data. Finally, above T_N = 165 K, the *M(H)* data are completely linear, confirming that the samples are paramagnetic above this temperature. Note that there is a slight splitting in the hysteresis loops at high temperature near -7 T. This feature is probably due to a slight rotation or re-alignment of the sample or sample holder, caused by the temperature and cycling of the field. For this reason, the (less interesting) paramagnetic data were acquired first.

The following Sections of this Chapter provide an analysis of data extracted from these hysteresis loops, such as ordering temperatures, and critical and coercive fields. A more complete interpretation is presented in Chapter 5.

4.4 Spontaneous Ferromagnetic Transition

Determination of T_C

All samples exhibit magnetic hysteresis at low temperatures with both a well-defined remanent magnetization and a well-defined coercive field. This confirms that the b-axis-oriented Dy samples are ferromagnetic below a specific temperature T_C which differs from sample to sample. The FM/AF transition occurs in bulk Dy at a Curie temperature of 85 K. However, a determination of the true Curie temperature for most magnetic systems is rendered difficult by the irreversibility of magnetization [3]. In a measurement of *M(T)*, T_C is identified by a splitting between the ZFC and FC branches; however, as discussed above, cooling the sample in zero field causes the spontaneous formation of a magnetic domain structure which varies from sample to sample and run to run. Isothermal hysteresis measurements of *M(H)* similarly suffer from irreversibility. For bulk Dy and c-axis-oriented thin film Dy, T_C was conveniently defined in the limit that H_C vanishes, but for our samples H_C is temperature-independent. Owing to these difficulties, Arrott diagrams (scaled magnetization vs. scaled applied field) are often used to accurately deduce the true Curie temperature [4].

In the present work, the numerical values of T_C were obtained by performing careful *M(H)* hysteresis measurements in a sequence of temperatures near T_C, to clearly identify the point at which the remanent magnetization vanishes. These are generally consistent with the irreversibility (splitting) temperature extracted from the *M(T)* data presented in Figure 4.1; however, in some cases a splitting superimposed on the ZFC/FC data, due to the parasitic ferromagnetic Zr contaminant, makes difficult the accurate extraction of T_C from ZFC/FC data alone.

For completeness, note that calculated hysteresis loops presented in Chapter 6 suggest that a ferromagnetic system can exhibit $M_R \approx 0$. Further measurements such as neutron diffraction are needed to fully confirm that the samples are ferromagnetic below T_C. Moreover, a coexistance of the FM and AF states has been reported in some systems, including c-axis-oriented Dy; such a coexistance is predicted by the Clausius-Clapyron relation for a constrained, first-order phase transition, depending on the difference in latent heats. Considering the properties of bulk Dy, however, and also ZFC/FC measurements, the association of T_C with $M_R = 0$ is not unreasonable.

Magnetic Phase Diagram

Measurements of T_C as a function of strain for all the samples are shown in Figure 4.5. This is in fact the magnetic phase diagram for b-axis-oriented Dy as a function of strain in zero applied field. Three important features are evident. First, the lowest critical temperature occurs for unstrained Dy and this temperature of 78 K is slightly *lower* than that observed for bulk Dy (85 K). Second, the critical temperature increases with increasing strain, both compressive and tensile. Third, the strain dependence of the critical temperature is approximately linear, with a weaker strain dependence on the compressive side.

The temperature-dependence of T_C for these b-axis-oriented Dy samples is a striking departure from what is observed for c-axis-oriented rare earths, in which T_C depends monotonically on strain. T_C is enhanced for c-axis-oriented Dy grown under compressive strain, on Lu and related systems, and it is reduced for c-axis-oriented Dy grown under tensile strain, on Y and related systems. In the case of c-axis Dy on Y in zero applied field, the ferromagnetic phase is completely suppressed. In the present work, the variation of critical temperature with strain is associated with the way epitaxial strain and clamping modifies the internal magneoelastic energy. Chapter 5 presents a unified model of magnetic ordering in epitaxial, thin film Dy, which conforms to the observed behavior of both c-axis and b-axis epitaxial systems.

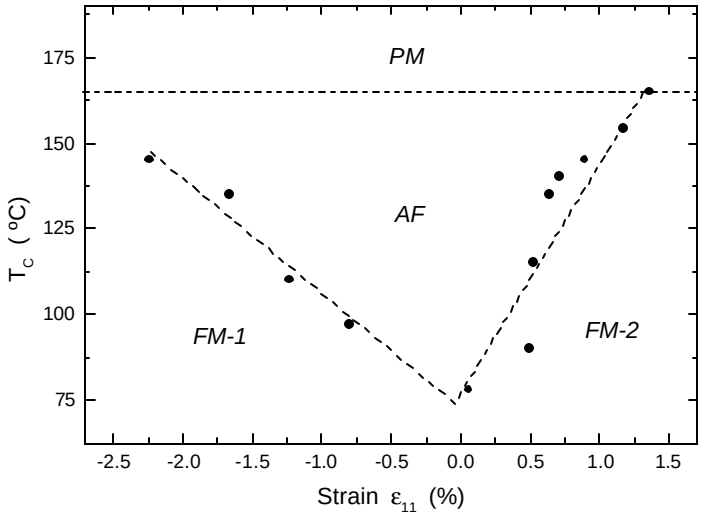

Figure 4.5: The magnetic phase diagram at H=0. The phase boundary between the ferromagnetic (FM) , antiferromagnetic (AF), and paramagnetic (PM) phases is shown. The labels FM-1 and FM-2 denote FM order but different axes of magnetization (see text).

4.5 Field-Induced Ferromagnetic Transition

The hysteresis loops with zero remanence observed in this research exhibit an abrupt kink at a critical field, H_C. This inflection marks a sudden change in the slope of $M(H)$, which identifies a change in the magnetic ordering process induced by the applied field. Magnetization measurements for bulk Dy, discussed in Chapter 1, as well as c-axis-oriented thin film Dy, display similar critical fields. For bulk Dy, H_C has been identified with a direct AF/FM phase boundary for temperatures below 130 K, and with the onset of a magnetic "fan" phase for temperatures above 130 K [5],[6][7]. The fan states occur when an applied magnetic field can partially collapse the helical antiferromagnetic structure into a ferrimagnetic state [8].

The observed hysteresis loops show two important features. First, the critical field H_C does not depend appreciably on temperature. In bulk Dy, H_C changes by over 1 T across the antiferromagnetic phase. As shown in Figure 4.6 for epitaxial b-axis-oriented Dy, there is no appreciable change of H_C with temperature. This temperature-independence is characteristic of all samples. Second, the critical field depends strongly

on strain. Figure 4.7 presents partial hysteresis loops *M(H)* taken at T = 130 K for all samples that are antiferromagnetic at that temperature, so that the strain dependence of the critical field can be seen clearly. This strain dependence is presented explicitly in Figure 4.8. The critical field H_C increases with increasing compressive strain, indicating that a progressively stronger applied field is necessary to induce the abrupt transition to ferromagnetic alignment.

4.6 Magnetic Anisotropy

Chapter 1 introduced the idea of anisotropic magnetic interactions and specifically the fact that many terms in the magnetic Hamiltonian exhibit preferred directions of lowest energy. The net effect of these terms governs the extent to which an external field can induce magnetization, and this determines the shape of the hysteresis curve.

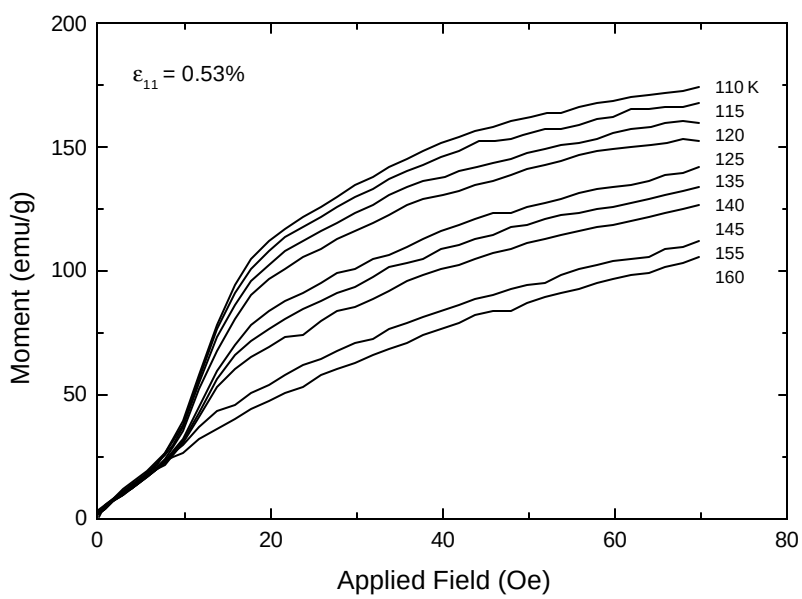

Figure 4.6. Partial M(H) hysteresis loops for temperatures in the antiferromagnetic phase of the sample with ε_{11} =0.53%. This temperature-independence of H_C is typical for all samples.

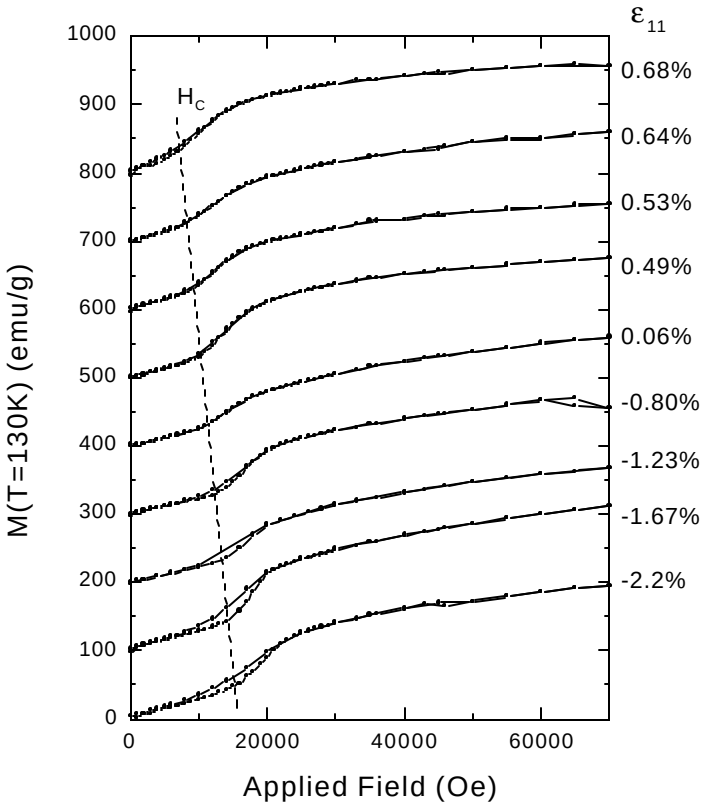

Figure 4.7. Partial *M(H)* hysteresis loops at T=130 K for all samples antiferromagnetic at this temperature. There is a pronounced dependence of the critical field H_C for ferromagnetic alignment on strain.

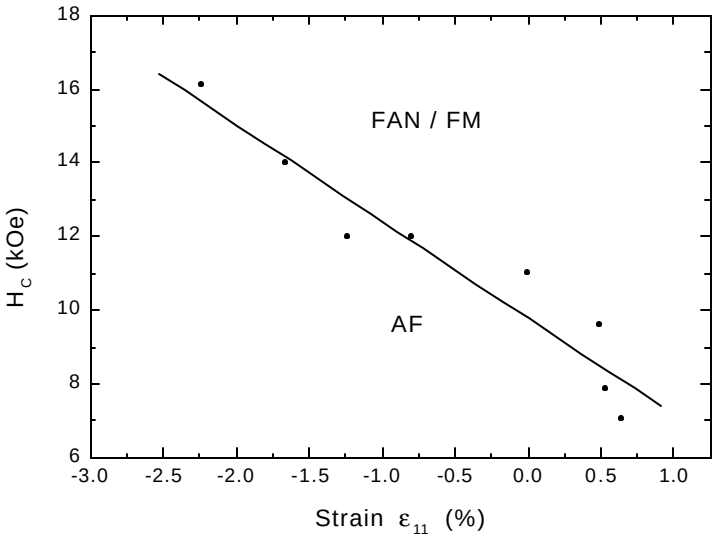

Figure 4.8. The strain-dependence of the critical field H_C in b-axis-oriented Dy samples. The data were obtained from *M(H)* at T=130K, but H_C itself has no appreciable temperature dependence.

Figure 4.9 shows hysteresis loops taken at 10 K. As the in-plane strain of the sample is changed from compressive (Lu) to tensile (Y), the hysteresis loops progressively "square up." Evidently, stretched b-axis Dy is more easily magnetized in-plane than compressed Dy. This suggests that the in-plane $[11\bar{2}0]$ axis changes from an easy axis of magnetization to a hard axis, depending on the strain. It will become apparent in Chapter 5 why this happens.

To further study the anisotropy, hysteresis loops were obtained with the field applied along the out-of-plane $[1\bar{1}00]$ axis. Hysteresis loops for this field direction are presented in Figure 4.10. Viewed as a function of strain these loops present almost the opposite trend in shape from those collected with H along the in-plane $[11\bar{2}0]$ axis. However, they do not become quite as square for most compressed Dy samples. These measurements are consistant with an in-plane $[11\bar{2}0]$ easy magnetization axis for stretched Dy. However, the easy axis for compressed Dy is not likely to be the out-of-plane $[1\bar{1}00]$ axis, but rather canted along an out-of-plane $[11\bar{2}0]$ direction.

The large difference between the magnetocrystalline anisotropy constants K_2 and K_6^6, discussed in Chapter 1, suggests that the in-plane [0001] axis is the overall hard magnetization axis. To verify this, measurements were performed with the field parallel to this direction with the results shown in Figure 4.11. Interestingly enough, the magnetization acquired at the highest fields of ±7 T is nearly 30% of the saturation moment for bulk Dy, which is somewhat larger than would be expected for $K_6^6 / K^2 \approx 10^{-2}$. This suggests that additional effects, such as dipolar coupling of domains, may make important contributions to the magnetization process.

These qualitative results concerning the observed anisotropy are fully corroborated in Chapter 5 by a quantitative calculation of the full magnetic anisotropy, using all terms of the magnetic Hamiltonian discussed in Chapter 1.

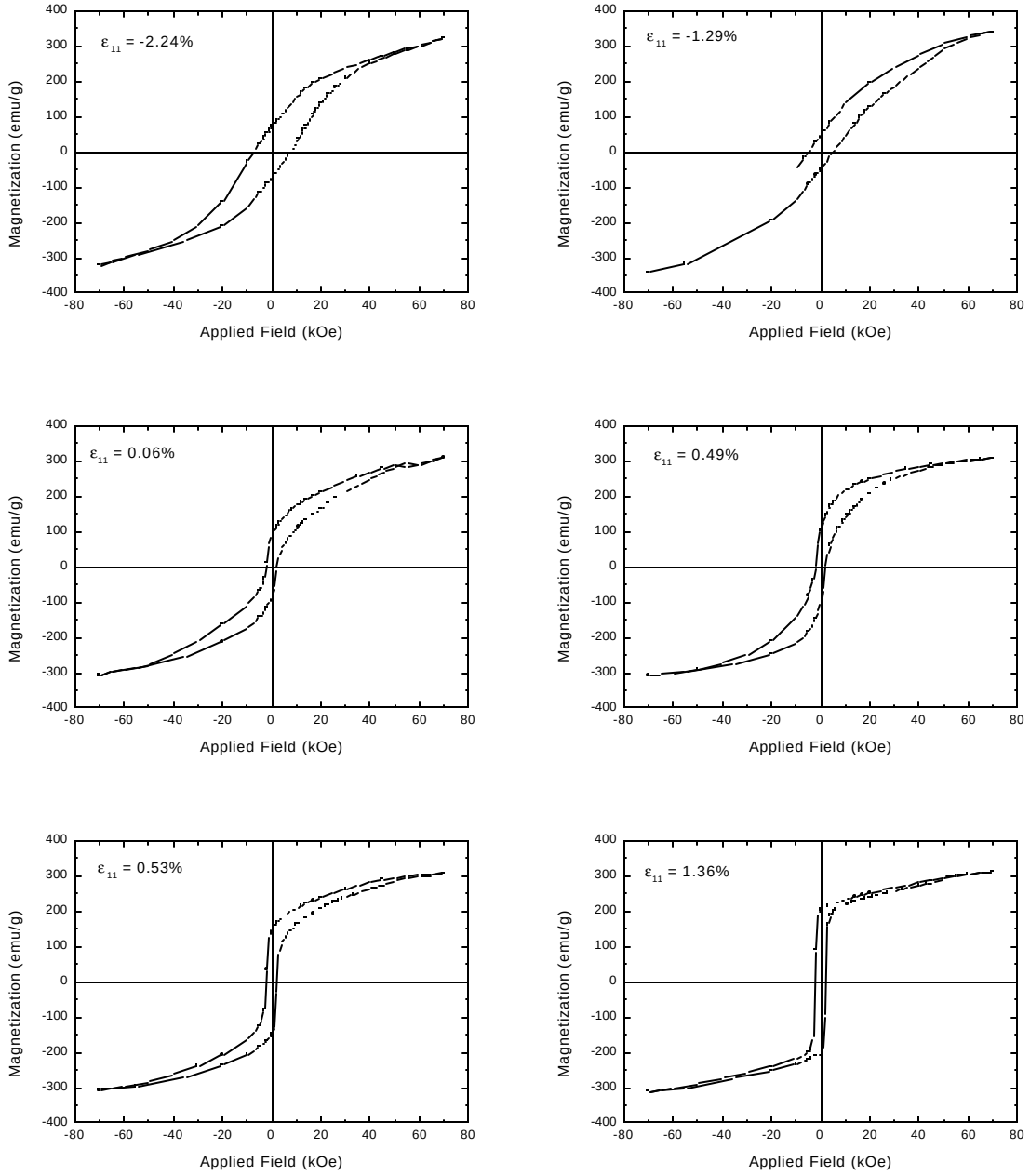

Figure 4.9: *M(H)* hysteresis loops collected for b-axis-oriented samples at 10K, with the field along the in-plane a-axis. The loops progressively "square-up" as the easy magnetization axis aligns with the field direction, with increasing tensile strain.

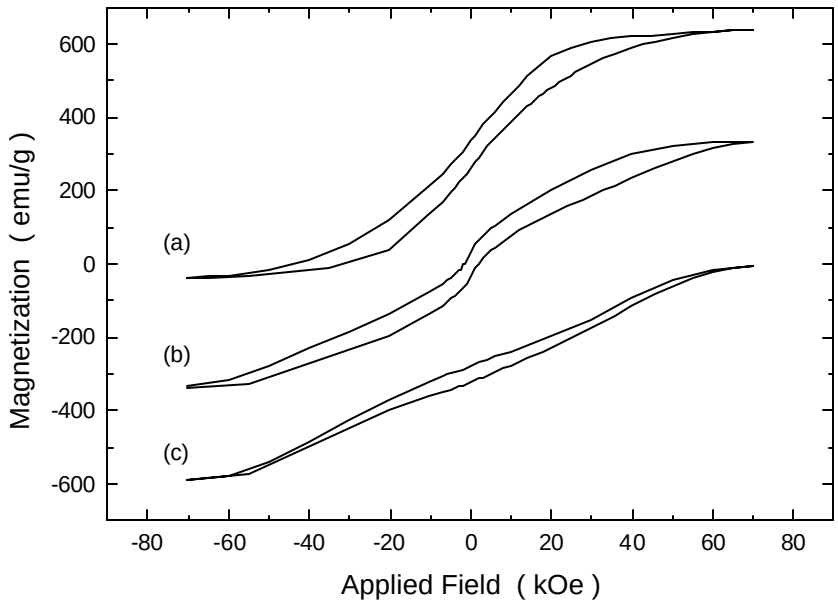

Figure 4.10. Hysteresis loops for (a) compressed, (b) unstrained, and (c) stretched b-axis-oriented Dy, with the applied field along the out-of-plane b-axis.

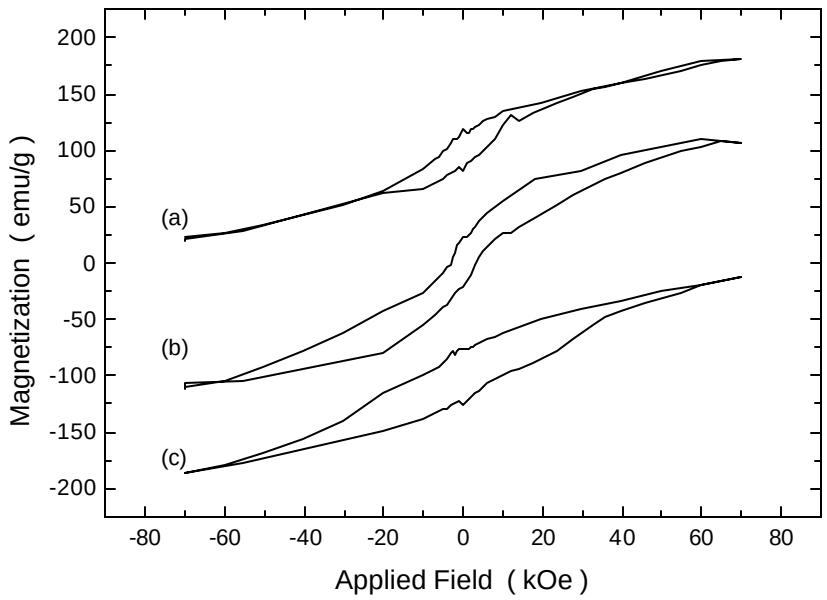

Figure 4.11. Hysteresis loops for (a) compressed, (b) unstrained, and (c) stretched b-axis-oriented Dy, with the applied field along the in-plane c-axis.

4.7 Paramagnetism

Néel Temperature

The Néel temperature is easily extracted from *M(T)* using the cusp in the susceptibility as described in Ref. [9], and it is found to be about 165 K for all samples, with no variation with strain or other parameters. The hysteresis loops show that the magnetization varies linearly with applied field above 165 K, thereby confirming that the Dy samples are paramagnetic for higher temperatures. This is significantly below the value T_N = 178 K observed for bulk Dy and for c-axis-oriented thin films and superlattices.

It is mentioned in Chapter 3 that in addition to the 7 nm Dy films, compressed Dy films 50 nm and 100 nm thick were grown on pure Lu buffer layers. SQUID magnetometry revealed Néel temperatures of 172 K and 178 K for these two films, respectively, as shown in Figure 4.12. This clearly indicates a systematic variation of T_N with sample thickness.

The Néel temperature can be modified by changes in the magnetic coherence length. This is the case for many order-disorder transitions, because the energy change that accompanies a phase transition is the sum of the energies gained in the ordered volumes whose size is specified by the coherence length. There are several mechanisms that reduce coherence lengths, including roughness (structural or magnetic), interdiffusion, impurities, etc. Alternatively, the observed reduction in T_N could be a finite-size effect. These ideas are discussed more fully in Chapter 5.

Paramagnetic Susceptibility

In addition to the Néel temperature which identifies the AF/PM phase boundary, the paramagnetic state in bulk Dy is characterized by two paramagnetic Curie temperatures, $T_{C\|}$ and $T_{C\perp}$. These are normally extracted by linear extrapolation of $c^{-1}(T)$. The parasitic ferromagnetic background saturates at modest fields and is therefore easily subtracted from hysteresis loops. Since it is not feasible to subtract this effect from *M(T)* data directly, the determination of these parameters from $c^{-1}(T)$ is not possible.

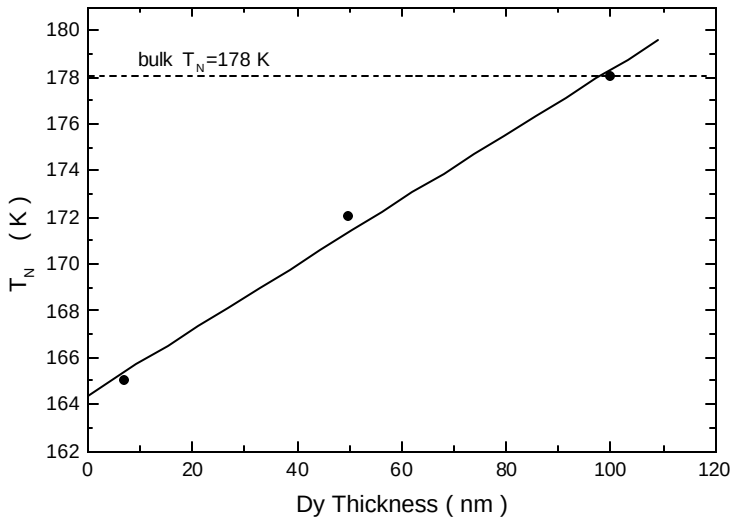

Figure 4.12. The variation in T_N, measured in an aligning field of 500 Oe, as a function of Dy layer thickness.

4.8 Coercive Field

Each sample exhibits a well-defined coercive field for $T<T_C$; this is the "switching" field necessary to reverse the sign of the magnetization. There are two observations to be made in this connection. First, the coercive field for all samples measured at 10 K is presented as Figure 4.13. As in-plane strain changes from compressive to unstrained, the coercive field is reduced. Then for tensile strain the coercive field becomes essentially constant. Because the stretched samples are spontaneously ferromagnetic at low temperatures, the magnetization reverses abruptly for very small applied fields, and the results are consequently noisy. Second, the coercive fields obtained for positive and negative applied fields are identical. This is consistent with hysteresis loops that are symmetric about H=0 and rules out any expected consequences of an external bias mechanism.

The coercive field may be an intrinsic magnetic property or may otherwise depend strongly on the degree to which magnetic domain walls are pinned. In Chapter 5, domain wall pinning is shown to be the most likely explanation for the present results. Semi-quantitative calculations of hysteresis loops in Chapter 6 provide corroborating evidence for this conclusion.

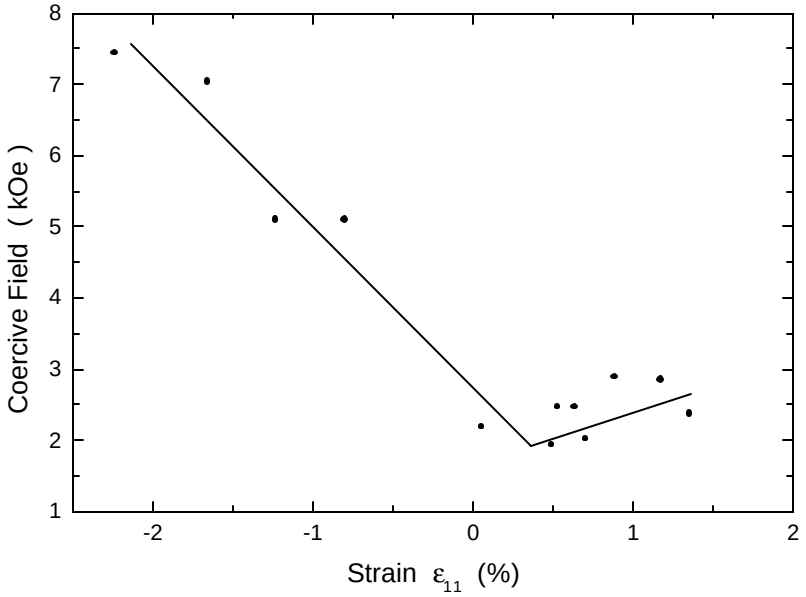

Figure 4.13. The measured coercive fields extracted from hysteresis loops. The small variation of the coercive field for tensile strain is likely to be random error, since the *M(H)* data were acquired with a 1 kOe step size. The straight lines are a guide to the eye.

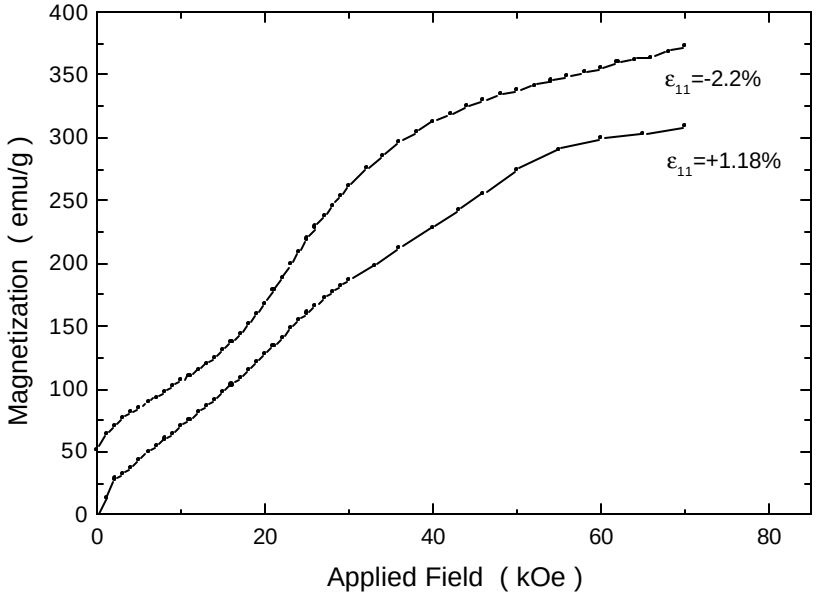

Figure 4.14. Hysteresis curves for previously unmagnetized b-axis-oriented Dy. The results for the compressed sample have been shifted by 50 emu / g for clarity.

4.9 Hysteresis Loops of Previously-Unmagnetized Samples

In order to study the initial stages of magnetic ordering as a function of applied field, hysteresis loops on previously-unmagnetized samples were collected in the following way. The samples were first cooled to the temperature of interest in zero applied field, and magnetization data were then collected as the field was increased.

Results for several samples are given in Figure 4.14. For compressed Dy, these curves show two distinct changes in slope, which point to changes of magnetic ordering or domain growth. For stretched Dy, the slope is essentially linear until saturation. In a discussion of these curves in Chapter 6, the models of magnetic ordering and hysteresis loops are described.

4.10 Magnetic Relaxation Measurements

Thus far the reported magnetic properties of b-axis-oriented Dy were probed first by temperature-dependent measurements of magnetization *M(T)* in small aligning fields, and second by isothermal hysteresis measurements *M(H)* in strong applied fields. This section addresses a different class of experiments, which investigate the time-dependent response of the samples to applied field at different temperatures.

High-Temperatures: Magnetic Aftereffect

A compressively-strained sample with ε_{22}=-1.66%, previously shown to possess distinct FM and AF states for *H=0,* was cooled in zero field to a desired temperature and a magnetic field of 1 T was subsequently applied. The net magnetization of the sample was then recorded during a seven hour period and this procedure was later repeated for other temperatures. The time-dependence of the magnetization for various temperatures is displayed in Figure 4.15.

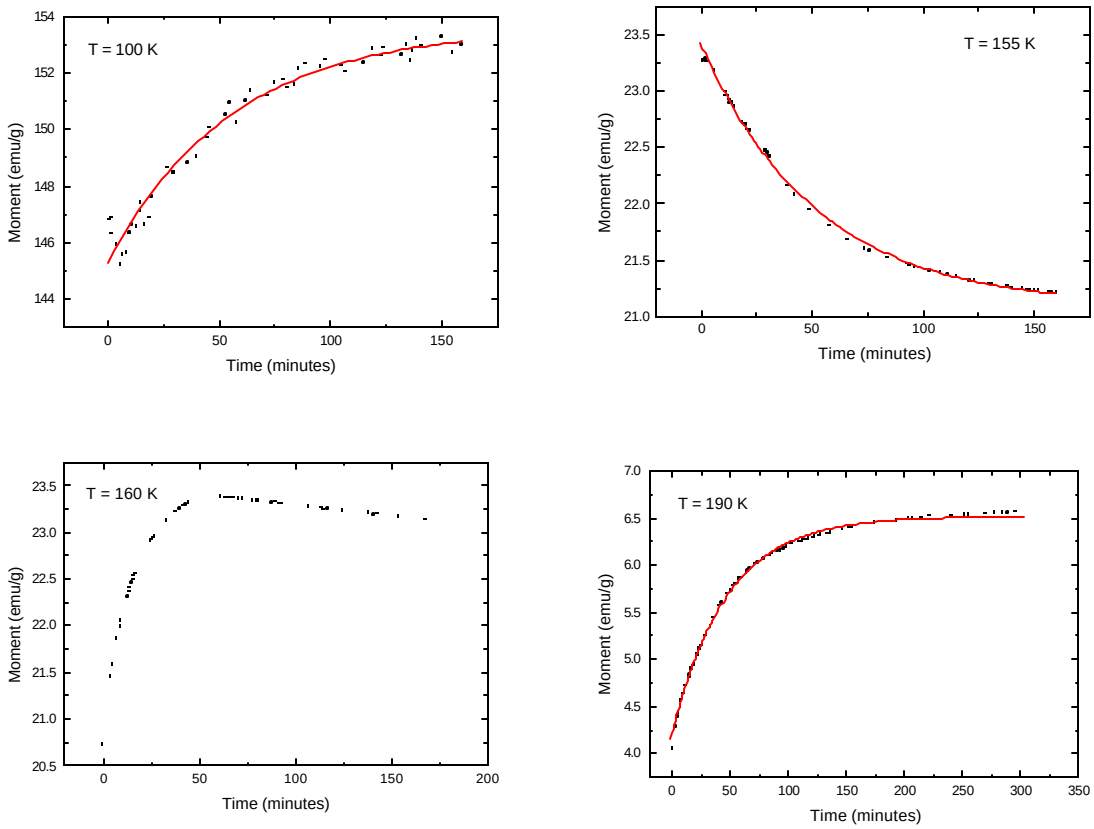

Figure 4.15. Time dependence of the magnetization for a sample with ε_{22}=-1.66%, recorded after the sample was cooled in zero field, immediately followed by the application of a 1T field. (Top left) T=35 K, in the FM state, showing that the magnetization increases with time. (Top right, bottom left) T=155 K and T = 160 K, field-cooled into the AF state. The magnetization abruptly increases and then slowly decreases. This shows that the applied field of 1 T generates metastable states. (Bottom right) T=190 K, the paramagnetic region.

In the FM and PM regimes the time-dependence of the magnetization can be fitted, although not exactly, by an exponential function of temperature. The exponential decay times extracted from fits to the data are shown as Figure 4.16. The fact that the magnetization increases with time to saturation is as expected: modified energy states develop as the applied field is ramped from H = 0 to H = 1 T, and the magnetization increases with time as these new configurations occur by domain growth, coherent rotation of single domains, or both. In the PM regime there is no long-range magnetic order and the magnetization therefore shows no strong dependence on temperature. (It is interesting to mention in this context the suggestion that a “vortex” phase occurs in the paramagnetic

region near T_N in bulk Dy [10], characteristic of a Kosterlitz-Thouless transition in the 2D XY model [11]. It is unlikely that any such phase can persist in thin film Dy, with less structural perfection, and if it does it is unlikely to become visible within the 10^1 s - 10^5 s time scale probed in our experiments.)

In the AF regime the time-dependence of magnetization is more complicated. The magnetization shown in Figure 4.15 rises abruptly to a maximum value and then slowly decreases to its equilibrium value. Recall that the field of 1 T used here is approximately the critical field H_C required for the field-induced AF/FM transition. It therefore appears that this unusual time dependence stems from a field-induced, metastable energy configuration, attributed to the proximity of H to the critical field. To provide more information about this region, measurements were repeated using applied fields both greater and less than H_C. In both cases the magnetization increased exponentially with time, as expected. In principle, it is possible that near complete relaxation measurements performed with greater precision both in temperature and applied field could be employed to probe the structure of the FM/AF phase boundary in greater detail.

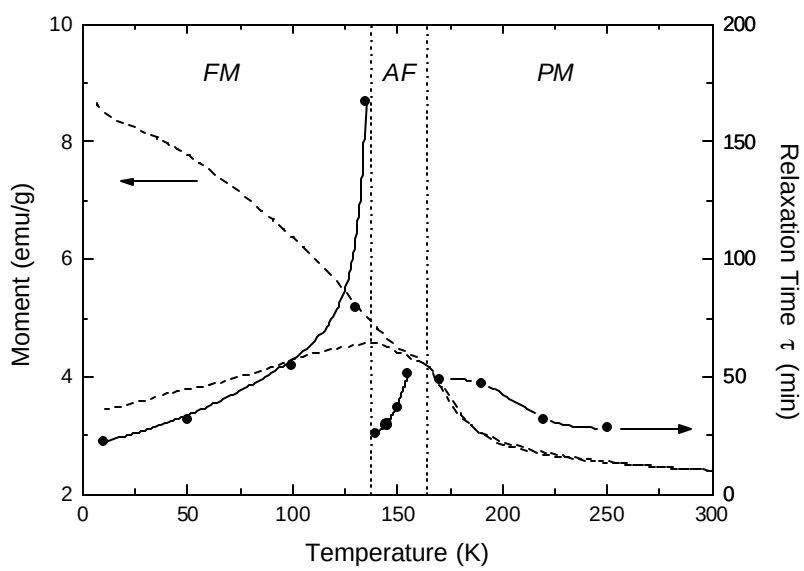

Figure 4.16. The temperature-dependence of the magnetic relaxation time for the magnetization, superimposed on the ZFC/FC data for the sample, for clarity.

Low-Temperatures: Possible Quantum Tunneling

Additional relaxation measurements on the sample with ε_{11}=-1.66% and on a second sample with tensile strain ε_{11}=+0.89% were made to investigate the low temperature behavior, where a possible crossover from thermally-activated (TA) to quantum tunneling (QTM) regimes can occur. The low-temperature relaxation data for these samples are presented as Figure 4.17. It is clear from the linearity of M vs. log T that these data are well-described by [3],[12]

$$M(t) = C - S\log(t/t) \qquad (1)$$

The magnetic viscosity S is defined by [13],[14],

$$S = dM/d\log t \qquad (2)$$

Figure 4.18 shows the temperature-dependent magnetic viscosity for these two samples. Three important features are apparent. First, the viscosity decreases with decreasing temperature until about T_c^* = 10 K, below which the viscosity is constant or slightly increasing. This identifies two regimes of temperature which have distinct magnetic ordering processes. Second, a linear fit to the high-temperature viscosity extrapolates to a finite, positive viscosity at zero temperature, suggesting that the high-temperature kinetics would not be completely frozen out at T = 0. This is observed in many instances of magnetic quantum tunneling. Third, there is no difference in T_c^* between the samples with tensile and compressive strain. Note that the vertical offset of these curves is in fact expected, since samples with different strain will have different net magnetization in applied fields less than saturation.

Whether these data indicatate the crossover from a thermal-activation regime to a quantum-tunneling regime, or else indicate some other process or phase transition, is discussed further in Chapter 5.

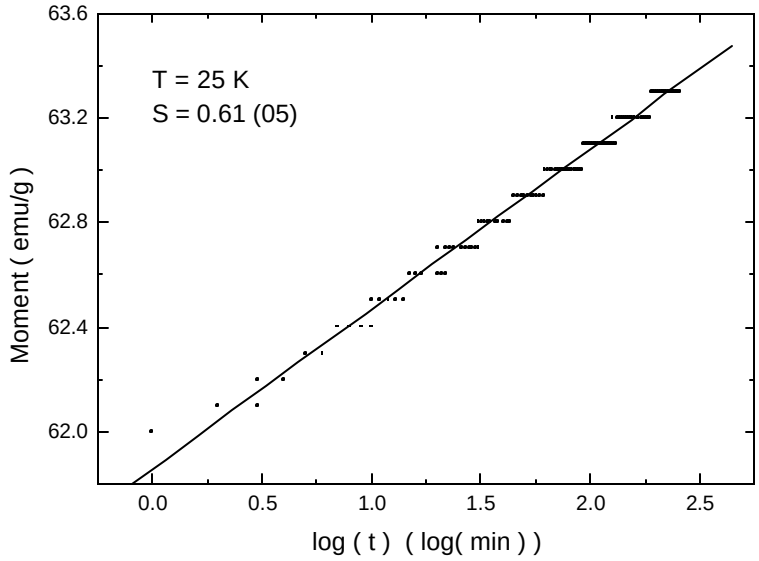

Figure 4.17. Magnetic relaxation in the sample with e_{11}=-1.66%, obtained at low temperature. Since the data are linear in log(t), it is clear these are well-characterized by the magnetic viscosity, defined in Eq. (2).

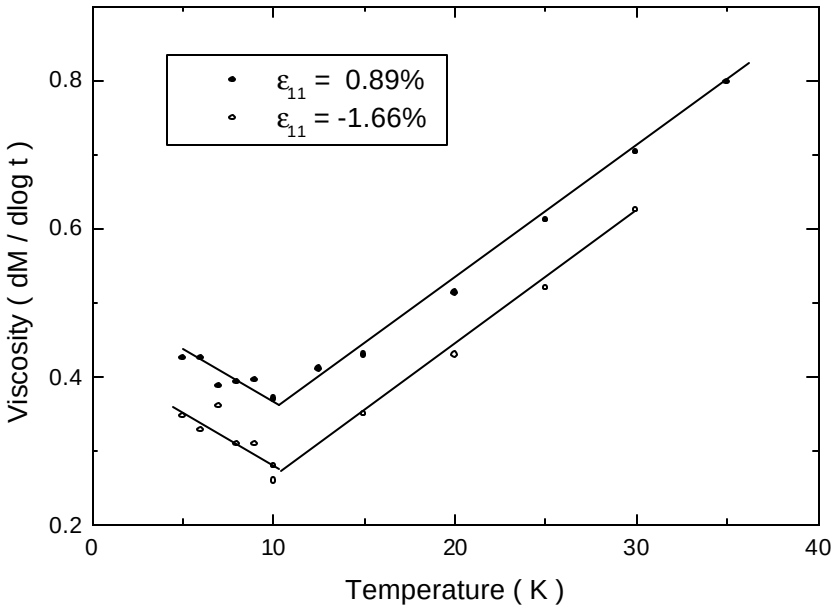

Figure 4.18. The magnetic viscosity as a function of sample temperature, obtained by linear fits to the viscosity data for samples with compressive and tensile strain.

4.11 Summary of Magnetic Properties

A series of clamped, strained, b-axis-oriented 7 nm Dy thin films, as well as 50 nm and 100 nm thin films, were investigated by SQUID magnetometry. Extensive temperature-dependent (ZFC/FC) magnetization data as well as isothermal hysteresis loops were collected. The main observations from these measurements are summarized as follows:

1. The direction of easy magnetization is strain-dependent. For tensile strain it is along the in-plane $[11\bar{2}0]$ axis, but for compressive strain it is canted towards the out-of-plane direction $[11\bar{2}0]$ directions.

2. The antiferromagnetic/paramagnetic phase boundary is constant at a Néel temperature T_N = 165 K for all 7 nm samples. With increasing layer thickness T_N achieves the bulk value of 178 K for a compressed Dy film, 100 nm thick.

3. The temperature at which the samples order ferromagnetically in zero field increases with increasing strain for both tensile and compressive strain, in contrast to monotonic dependence for c-axis-oriented rare earths.

4. The coercive field is constant for samples under tensile strain, and it increases with decreasing compressive strain.

5. The critical fields H_C required to induce ferromagnetic ordering decrease with increasing tensile strain, which shows that this direction becomes an increasingly easy magnetization axis. The critical fields are temperature-independent, in contrast to bulk or c-axis-oriented Dy, because the reduction of hexagonal symmetry introduces magnetoelastic energy barriers which are large and temperature-independent.

6. Studies of time-dependent magnetic relaxation were also carried out. These were conducted at high temperature to examine the magnetic aftereffect, and at low temperature to explore a possible crossover to quantum tunneling. The results of these measurements are as follows:

   a. The time-dependent magnetic relaxation reveals metastable states near the threshold H_C for induced ferromagnetic ordering. For applied fields well above and below this threshold, the ordering kinetics are exponential.

b. The magnetic ordering rate changes abruptly below 10 K, signaling the onset of either quantum tunneling or some unknown activation process. There is no dependence of ordering rate on strain in either regime.

Chapter 5 provides a quantitative interpretation for each of these observations. A self-consistent model of magnetic ordering, applicable to both b-axis-oriented and c-axis-oriented Dy, is developed there.

References

[1] The precise identification of the splitting temperature is rendered difficult by the ferromagnetic impurity contribution, which superimposes a splitting between the ZFC and FC legs of *M(T)* for all temperatures.

[2] M. B. Salamon, private communication.

[3] A. Aharoni, *Introduction to the theory of ferromagnetism* (Clarendon Press, Oxford, 1996).

[4] The idea is to use mean field theory, expanding the Brillouin function whose argument is small in the vicinity of the Curie temperature. The original work was an internal, unpublished General Electric report. For an excellent description of problems and difficulties inherent to the Arrott method, see A. Aharoni, *Introduction to the theory of ferromagnetism* (Clarendon Press, Oxford, 1996).

[5] J. J. Rhyne, S. Foner, E. J. McNiff, R. Doclo, *J. App. Phys.* **39**, 892-893 (1968).

[6] R. M. Bozorth, R. J. Gambino, A. E. Clark, *J. App. Phys.* **39**, 883-886 (1968).

[7] D. R. Behrendt, S. Legvold, F. H. Spedding, *Phys. Rev.* **109**, 1544-1547 (1957); J. F. Elliott, S. Legvold, F. H. Spedding, *Phys. Rev.* **94**, 1143-1145 (1954).

[8] M. Akhavan, H. A. Blackstead, P. L. Donoho, *Phys. Rev. B* **8**, 4258-4261 (1973).

[9] B. D. Cullity, *Introduction to magnetic materials* (Addison-Wesley, Reading, 1972).

[10] E. B. Amitin, V. G. Bessergenev, Y. A. Kovalevskaya, *J. Phys. F: Met. Phys.* **14**, 2935-2942 (1984); E. B. Amitin, V. G. Bessergenev, Y. A. Kovalevskaya, *Fiz. Tverd. Tela* (Leningrad) **26**, 1044-1048 (1984); E. B. Amitin, V. G. Bessergenev, Y. A. Kovalevskaya, *Zh. Eksp. Teor. Fiz.* **84**, 205-214 (1983). An excellent theoretical description of the vortex phase is provided by A. M. Kosevich, V. P. Voronov, and I. V. Manzhos, *Sov. Phys. JETP* **57**, 86-92 (1983).

[11] V. G. Bessergenev, V. V. Gogava, Y. A. Kovalevskaya, A. G. Mandzhavidze, V. M. Fedorov, S. I. Shilo, *Pis'ma Zh. Eksp. Teor. Fiz.* **42**, 412-414 (1985).

[12] E. Dan Dahlbert, D. K. Lottis, R. M. White, M. Matson, E. Engle, *J. App. Phys.* **76**, 6396-6400 (1994).

[13] L. Folks, R. Street, *J. App. Phys.* **76**, 6391-6395 (1994).

[14] R. Street, S. D. Brown, *J. App. Phys.* **76**, 6386-6390 (1994).